Article

A next-generation, histological atlas of the human brain and its application to automated brain MRI segmentation

Adrià Casamitjana[1,2], Matteo Mancini[1,3,4], Eleanor Robinson[1], Loïc Peter[1], Roberto Annunziata[1], Juri Althonayan[1], Shauna Crampsie[1], Emily Blackburn[1], Benjamin Billot[1,5], Alessia Atzeni[1], Oula Puonti[6,7], Yaël Balbastre[1,7], Peter Schmidt[8], James Hughes[8], Jean C Augustinack[7], Brian L Edlow[7,9], Lilla Zöllei[7], David L Thomas[10,11], Dorit Kliemann[12], Martina Bocchetta[10,13], Catherine Strand[14], Janice L Holton[14], Zane Jaunmuktane[14], & Juan Eugenio Iglesias[1,5,7,*]

1 Department of Medical Physics and Biomedical Engineering, University College London, London, United Kingdom
2 Research Institute of Computer Vision and Robotics, University of Girona, Girona, Spain
3 Department of Cardiovascular, Endocrine-Metabolic Diseases and Aging, Italian National Institute of Health, Rome, Italy
4 Cardiff University Brain Research Imaging Centre, Cardiff University, Cardiff, United Kingdom
5 Computer Science and Artificial Intelligence Laboratory, Massachusetts Institute of Technology, Cambridge, MA, United States
6 Danish Research Centre for Magnetic Resonance, Centre for Functional and Diagnostic Imaging and Research, Copenhagen University Hospital - Amager and Hvidovre, Copenhagen, Denmark
7 Athinoula A. Martinos Center for Biomedical Imaging, Massachusetts General Hospital and Harvard Medical School, Boston, MA, United States
8 Advanced Research Computing Centre, University College London, London, United Kingdom
9 Center for Neurotechnology and Neurorecovery, Department of Neurology, Massachusetts General Hospital and Harvard Medical School, Boston, MA, United States
10 Dementia Research Centre, Department of Neurodegenerative Disease, UCL Queen Square Institute of Neurology, University College London, London, United Kingdom
11 Neuroradiological Academic Unit, Department of Brain Repair and Rehabilitation, UCL Queen Square Institute of Neurology, University College London, London, United Kingdom
12 Department of Psychological and Brain Sciences, University of Iowa, Iowa City, IA, United States
13 Centre for Cognitive and Clinical Neuroscience, Division of Psychology, Department of Life Sciences, College of Health, Medicine and Life Sciences, Brunel University London, United Kingdom
14 Queen Square Brain Bank for Neurological Disorders, Department of Clinical and Movement Neurosciences, UCL Queen Square Institute of Neurology, University College London, London, United Kingdom

* Correspondence: jiglesiasgonzalez@mgh.harvard.edu

Abstract: Magnetic resonance imaging (MRI) is the standard tool to image the human brain *in vivo*. In this domain, digital brain atlases are essential for subject-specific segmentation of anatomical regions of interest (ROIs) and spatial comparison of neuroanatomy from different subjects in a common coordinate frame. High-resolution, digital atlases derived from histology (e.g., Allen atlas [3], BigBrain [4], Julich [5]), are currently the state of the art and provide exquisite 3D cytoarchitectural maps, but lack probabilistic labels throughout the whole brain. Here we present *NextBrain*, a next-generation probabilistic atlas of human brain anatomy built from serial 3D histology and corresponding highly granular delineations of five whole brain hemispheres. We developed AI techniques to align and reconstruct ~10,000 histological sections into coherent 3D volumes, as well as to semi-automatically trace the boundaries of 333 distinct anatomical ROIs on all these sections. Comprehensive delineation on multiple cases enabled us to build an atlas with *probabilistic* labels throughout the whole brain. Further, we created a companion Bayesian tool for automated segmentation of the 333 ROIs in any *in vivo* or *ex vivo* brain MRI scan using the *NextBrain* atlas. We showcase two applications of the atlas: automated segmentation of ultra-high-resolution *ex vivo* MRI and volumetric analysis of brain ageing based on ~4,000 publicly available *in vivo* MRI scans. We publicly release the raw and aligned data (including an online visualisation tool), probabilistic atlas, and segmentation tool. By enabling researchers worldwide to analyse brain MRI scans at a superior level of granularity without manual effort or highly specific neuroanatomical knowledge, *NextBrain* will accelerate our quest to understand the human brain in health and disease.

Magnetic resonance imaging (MRI) is arguably the most important tool to study the human brain *in vivo*. Its exquisite contrast between different types of soft tissue provides a window into the living brain across all ages without ionising radiation, making it suitable to healthy volunteers. Advances in magnet strength, data acquisition and image reconstruction methods [6-10] enable the acquisition of millimetre-resolution MRI scans of the *whole* brain in minutes. These scans can be acquired with different pulse sequences that image different tissue properties, including: neuroanatomy with conventional structural acquisitions [11]; brain activity (including functional connectivity and networks) with functional MRI based on blood oxygenation level dependent (BOLD) imaging [12]; vasculature with perfusion imaging and MR angiography [13-16]; or white matter fibres and microstructure with diffusion-weighted MRI [17,18].

As MRI became increasingly available in research settings in the late 1990s and early 2000s, neuroimaging packages emerged to analyse different types of MRI scans. Prominent examples include FreeSurfer [19], FSL [20], SPM [21], and AFNI [22], all of which are publicly available. These packages enable researchers to perform large-scale studies with thousands of scans [23-26] and chart the time course of healthy ageing, as well as a broad spectrum of brain diseases, such as Alzheimer's, multiple sclerosis, depression, and many others [27-30]. The tools have also enabled reproducibility, especially when combined with publicly available datasets such as the Alzheimer's Disease Neuroimaging Initiative [31], Human Connectome Project [32], Chinese Human Connectome Project [33], or UK BioBank [34].

A core component of these neuroimaging packages is digital brain atlases. These are reference brain images that are representative of a certain population and can comprise image intensities, neuroanatomical labels, or both. They are typically computed by averaging data from a large cohort of subjects [35], but they may comprise as few as a single subject – particularly when built from labour-intensive modalities like 3D histology, which entails combining a large amount of high-resolution histological sections [4]. Atlases enable aggregation of data from different subjects into a common coordinate frame (CCF), thus allowing analyses as a function of spatial location, e.g., group comparisons or regressions. Some atlases also integrate semantic data, which provide prior information for subject-specific analyses – for example, voxel-wise probabilities for brain regions, with image segmentation applications [36].

The atlases in neuroimaging packages are primarily built from *in vivo* MRI scans acquired at ~1mm isotropic resolution. This is also the case for many more modern atlases, such as the widespread HCP-MMP1 cortical atlas, built from multi-modal MRI data [37]. This resolution is sufficient to represent information at the level of gyri, sulci, and subcortical nuclei. However, ~1mm isotropic resolution is insufficient to study the brain at the subregion level, which is desirable as brain substructures are known from animal models and *postmortem* human studies to have different function and connectivity [38]. By enabling higher resolution, *ex vivo* MRI partly mitigates this problem [2,39-41], but still fails to visualise cytoarchitecture and resolve many boundaries between brain regions and subregions.

Compared with MRI, histology is a microscopic 2D modality with limited anatomical coverage that can visualise distinct aspects of cytoarchitecture using an array of stains. Combining serial histology with image registration (alignment) methods enables volumetric reconstruction of 3D histology [42]: by reversing the distortion that brain tissue undergoes during acquisition, one can reassemble a 3D shape that accurately resembles the original anatomy. 3D histology can be used to build histological atlases. Though much more labour-intensive than MRI-atlasing, histological atlases that consider cytoarchitecture have two major advantages: *(i)* providing a more detailed CCF; and *(ii)* the ability to segment MRI scans at the subregion level – with potentially higher sensitivity and specificity to detect brain alterations caused by brain diseases or measure treatment effects.

Previous efforts in whole-brain histological atlasing include BigBrain [4], Julich Brain [5], the Allen reference brain [3], and the Ahead brains [43]. BigBrain comprises ultra-high resolution, accurately reconstructed 3D histology of a single brain, with partial anatomical annotations. BigBrain paved the road for its followup Julich Brain [5], which aggregates data from 23 individuals with full cortical (but partial subcortical) annotations. The Allen reference brain has comprehensive anatomical annotations on high-resolution histology and is integrated with the Allen gene expression atlases, but only has delineations for a sparse set (N=106) of histological sections of a single specimen. The recent Ahead brain comprises quantitative MRI and registered 3D histology for two separate specimens. These have annotations for a few dozen structures, but they were obtained from the MRI with automated methods, rather than manually traced on the high-resolution histology.

While these histological atlases provide exquisite 3D cytoarchitectural maps, interoperability with other datasets (e.g., gene expression), and MRI-histology integration, there are currently no probabilistic atlases built from whole-brain histology of multiple specimens with exhaustive manual delineation. This precludes analyses such as Bayesian segmentation or CCF mapping of the whole brain at the subregion level, which would be highly beneficial complements to the capabilities of these projects.

In this article, we present *NextBrain*, a next-generation probabilistic atlas of the human brain built from

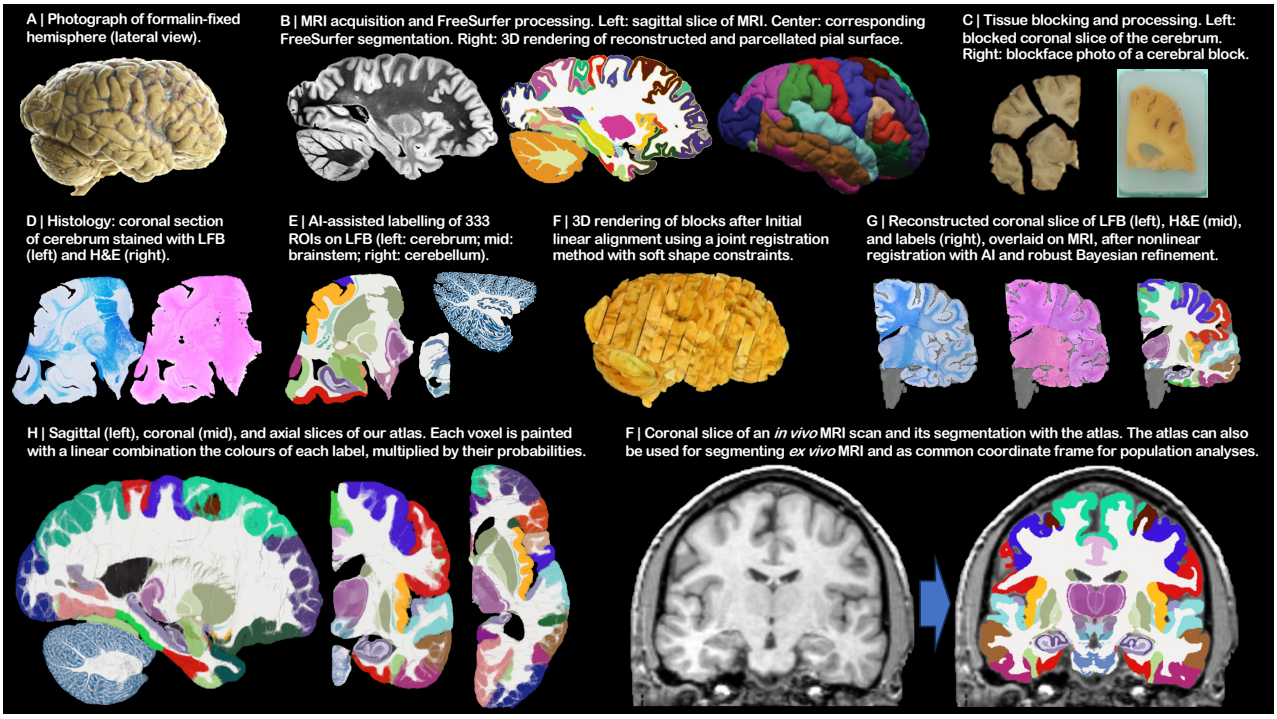

Fig. 1: NextBrain workflow. (A) Five human hemispheres were formalin fixed. (B) High-resolution MRI scans of the fixed hemispheres were acquired at 400µm isotropic resolution and processed with FreeSurfer 7.0 to extract and parcellate the cortex. (C) The hemispheres were dissected into blocks, processed into paraffin, and sectioned into 25µm slices with a microtome while taking blockface photographs. (D) Sections were stained with H&E and LFB every 250 or 500µm (depending on the anatomy; see details in Methods section) and digitised at 4µm resolution. (E) An AI method was used to semi-automatically label 333 brain regions on ∼5,000 LFB sections with reduced manual intervention. (F) A custom image alignment ("registration") method was used to build a preliminary 3D reconstruction of the photographs using the MRI as a reference; the photographs do not suffer from virtually any nonlinear distortion as they are taken prior to sectioning. (G) This registration is refined using the histology, which is nonlinearly distorted but has much better resolution and contrast, using a combination of AI and Bayesian techniques. The result is a joint 3D reconstruction of the H&E, LFB, MRI, and neuroanatomical labels. (H) The 3D reconstructed labels are used to build a probabilistic atlas with an unbiased algorithm. (I) The atlas can be used for automated Bayesian segmentation of the 333 regions using the code that we distribute with FreeSurfer.

comprehensively labelled, multi-modal 3D histology of five half brains. The full dataset comprises ∼10,000 sections stained with Hematoxylin and Eosin (H&E, which discerns cell nuclei vs cytoplasm) and Luxol Fast Blue (LFB, which enhances myelin). These sections were: *(i)* 3D-reconstructed with *ex vivo* MRI scans and image registration powered by artificial intelligence (AI); and *(ii)* densely segmented into 333 regions of interest (ROIs) with AI-enabled, semi-automated segmentation methods. *NextBrain* is distributed with a companion Bayesian tool for automated segmentation of MRI scans. The atlas, raw and registered images, online visualisation tool, segmentation method, and source code are all publicly available (see Data Availability section).

As the first densely labelled probabilistic atlas of the human brain built from histology, *NextBrain* enables brain MRI analysis at a level of detail that was previously not possible. The raw and registered images that were used to build the atlas are also freely available and are themselves an invaluable resource for MRI signal modelling or histology registration studies. Moreover, the data acquisition pipeline does not require highly specialised equipment (e.g., a full-brain microtome, as the Allen or Julich brains), thus enabling wide applicability.

Densely labelled 3D histology of five human hemispheres

The *NextBrain* workflow is summarised in Fig. 1 and detailed in the Methods section. The first result of the pipeline (panels A-G) is a multimodal dataset with human hemispheres from five donors (three right, two left), including half cerebellum and brainstem. Each of the five cases comprises accurately aligned high-resolution *ex vivo* MRI, serial histology (H&E and LFB stains), and dense ground truth segmentations of 333 cortical and subcortical brain ROIs.

Aligning the histology of a case is analogous to solving a 2,000-piece jigsaw puzzle in 3D, with pieces that are deformed by sectioning and mounting on glass slides, with occasional tissue folding or tearing. We solve this challenging problem with a custom, state-of-the-art image registration framework (Fig. 2) that has three crucial components: *(i)* a differentiable regulariser that minimises overlap of different blocks and gaps in between [44]; *(ii)* an AI registration method that uses contrastive learning to provide highly accurate alignment of corresponding brain tissue across MRI and histology [45]; and *(iii)* a Bayesian refinement technique

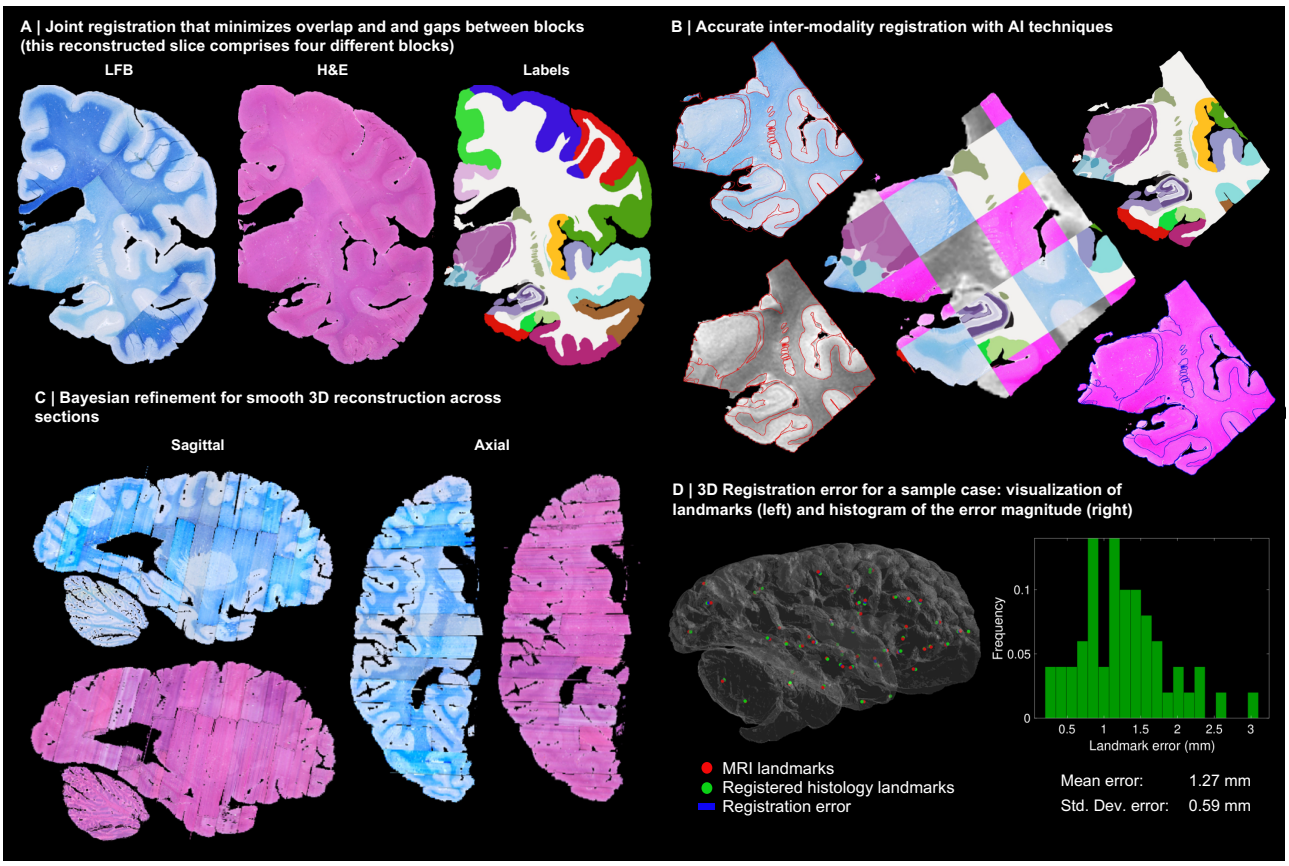

Fig. 2: 3D reconstruction of Case 1. (A) Coronal slice of the 3D reconstruction, which includes pixels from four different tissue blocks (noticeable from uneven staining); the joint registration minimizes overlap and gaps between blocks. (B) Our AI-enabled registration yields accurate alignment across MRI, LFB, and H&E. The contours of the ROIs are overlaid on the different modalities. The mosaic combines the three modalities and the segmentations. (C) Our Bayesian refinement algorithm ensures that the 3D reconstruction is smooth across histological sections, even in the presence of outliers in the registration due to, e.g., tissue folding and tearing. This is exemplified with sagittal and axial views of the cerebrum, which is cut in coronal plane. (D) Visualization of 3D landmark registration error (left) and histogram of its magnitude (right). Similar figures for the other four cases can be found in the Extended Data. The average landmark error across the five cases is 0.99mm.

based on Lie algebra that guarantees the 3D smoothness of the reconstruction across modalities, even in the presence of outliers due to tissue folding and tearing [46].

Qualitatively, it is apparent from Fig. 2 that a very high level of accuracy is achieved for the spatial alignment, despite the strong distortions present in the raw data. The regulariser effectively aligns the block boundaries in 3D (Figures 2A and 2C), with minor discontinuities across blocks (e.g., in the temporal lobe). When the segmentations from different blocks are combined (Fig. 2A, right), the result is a smooth composite slice of ROI segmentations.

The AI-enabled registration across MRI and histological stains is exemplified in Fig. 2B. Overlaying the main ROI contours on the different modalities reveals the highly accurate alignment of the three modalities (MRI, H&E, LFB), even in convoluted regions of the cortex and the basal ganglia. The mosaic of modalities also highlights the accurate alignment at the substructural level, e.g., subregions of the hippocampus.

Fig. 2C illustrates the smoothness that is achieved in the 3D reconstruction in orientations orthogonal to the plane of sectioning, without compromising the accuracy of the alignment to the reference MRI. This is due to the Bayesian refinement algorithm, which combines the best features of methods that: *(i)* align each section independently (high fidelity to the reference, but jagged reconstructions) and *(ii)* those that align sections to their neighbours (smooth reconstructions, but with "banana effect", i.e., straightening of curved structures). Quantitative results are presented in Fig. 2D, as well as in Extended Data Figures 1-4D in the online version. The registration error, evaluated with 250 manually placed pairs of landmarks, is 0.99 ± 0.51mm. This represents a ~50% reduction compared with our previous pipeline [47].

One important advantage of our method is that it does not require the highly specialised equipment needed for intact coronally sliced full-brain histological procedures used by select sites like the Allen Institute or Julich (full-brain microtome, custom glass slides, etc.). Instead, our method produces accurate 3D reconstructions from blocked tissue in standard-sized cassettes, sectioned with a standard microtome – thus enabling wide applicability.

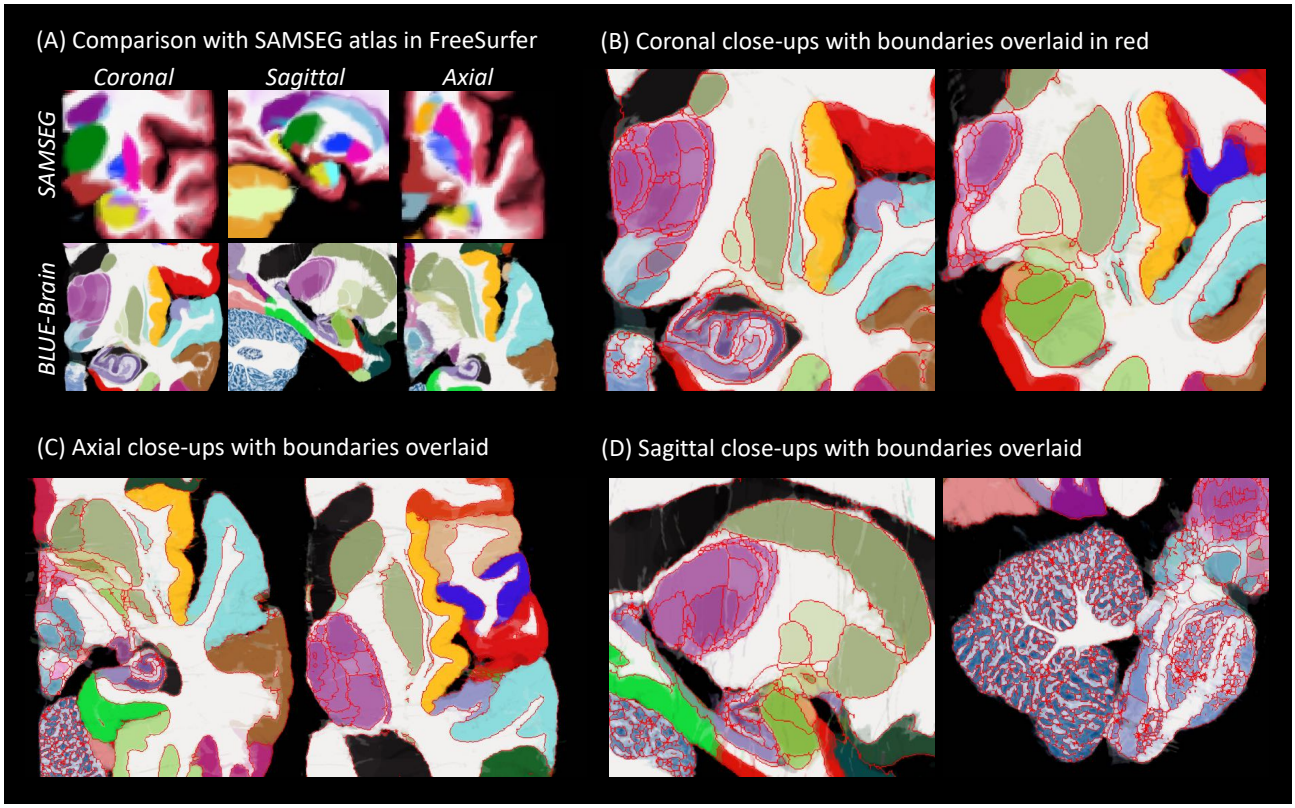

Fig. 3: *NextBrain* probabilistic atlas. (A) Portions of the NextBrain probabilistic atlas, compared with the whole brain probabilistic atlas of the Bayesian segmentation tool "SAMSEG" that is currently distributed with FreeSurfer; we note that NextBrain is sharper due to the lower number of cases. (B) Close-up of two coronal slices, focusing on the thalamus, hippocampus, and midbrain (left); and hypothalamus, amygdala, and basal ganglia (right). (C) Axial closeups focused on the midbrain, hypothalamus, basal ganglia, and hippocampus (left); and thalamus, basal ganglia, and caudate (right). (D) Sagittal close-ups, focusing on the thalamus, hippocampus, caudate, basal ganglia, and amygdala (left); and midbrain, brainstem, and cerebellum (right). The colour coding follows the convention of the Allen atlas [3], where the hue indicates the structure (e.g., thalamus in purple) and the saturation is proportional to the neuronal density. The colour at each voxel is a weighted sum of the colour corresponding to the ROIs that may occur at the voxel, weighted by the corresponding probabilities. The red lines separate ROIs based on the most probable label at each voxel.

The aligned dataset is freely available in our public repository (see Data Availability) and can be explored interactively at: github-pages.ucl.ac.uk/NextBrain. Supplementary Video 1 also illustrates the aligned data. The dataset includes: *(i)* the MRI at 400µm isotropic resolution; *(ii)* the aligned H&E and LFB histology digitised at 4µm resolution (with 250 or 500µm spacing, depending on the brain location); and *(iii)* the ROI segmentations, which were obtained with AI-assisted manual tracing [48], and which include 34 cortical labels (following the Desikan-Killiany atlas [49]) and 299 subcortical labels (following different atlas for different brain regions; see the Methods section below and the supplement). This public dataset enables researchers worldwide to conduct their own studies not only in 3D histology reconstruction, but also other fields like: high-resolution segmentation of MRI or histology [50]; MRI-to-histology and histological stain-to-stain image translation [51]; deriving MRI signal models from histology [52]; and many others.

A next-generation probabilistic atlas of the human brain

The labels from the five human hemispheres were co-registered and merged into a probabilistic atlas using an unbiased method that ensures that the result is not skewed towards any of the five cases [53]. The co-registration method is diffeomorphic to ensure preservation of the neuroanatomic topology (e.g., ROIs do not split or disappear in the deformation process).

Fig. 3 shows close-ups of orthogonal slices of the atlas, which models voxel-wide probabilities for the 333 ROIs on a 0.2mm isotropic grid. The resolution and detail of the atlas represents a substantial advance with respect to the SAMSEG atlas [54] currently in FreeSurfer (Fig. 3A). SAMSEG models 13 brain ROIs at 1mm resolution and is, to the best of our knowledge, the most detailed probabilistic atlas that covers all brain regions; more detailed atlases exist but only provide partial anatomical coverage [55,56].

Close-ups of slices of the atlas centred on representative brain regions are shown in Fig. 3B-D, with boundaries between the ROIs (computed from the maximum

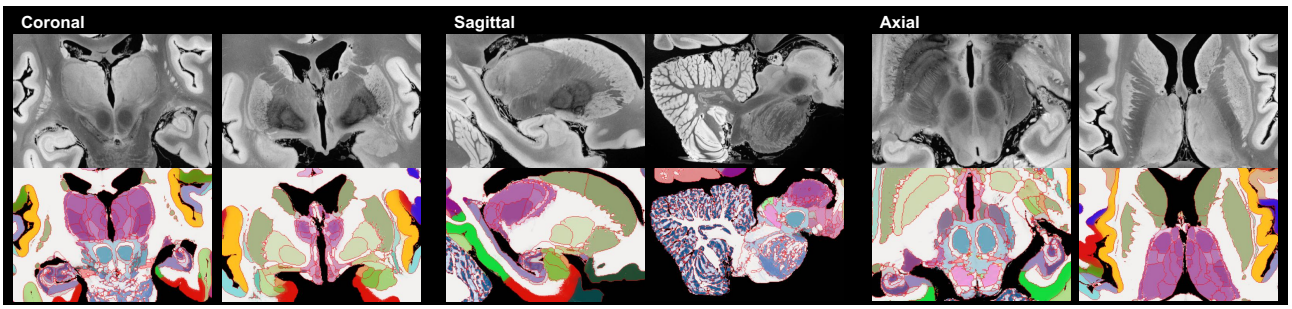

Fig. 4: Automated Bayesian segmentation of publicly available ultra-high resolution *ex vivo* brain MRI [2] using *NextBrain*. We show two coronal, sagittal, and axial slices of the MRI (top row) and their segmentations (bottom row). The MRI was resampled to 200µm isotropic resolution for processing. As in previous figures, the segmentation uses the Allen colour map [3], with boundaries overlaid in red.

likelihood segmentation) overlaid in red. These highlight the anatomical granularity of the new atlas, with dozens of subregions for areas such as the thalamus, hippocampus, amygdala, midbrain, etc. An overview of the complete atlas is shown in Supplementary Video 2, which illustrates the atlas construction procedure and flies through all the slices in axial, coronal, and sagittal view.

The probabilistic atlas is freely available as part of our segmentation module distributed with FreeSurfer. The maximum likelihood and colour-coded maps (as in Fig. 3) can also be downloaded separately from our public repository (see Data Availability). Developers of neuroimaging methods can freely capitalise on this resource, e.g., by extending the atlas via combination with other atlases or manually tracing new labels; or by designing their own segmentation methods using the atlas. Neuroimaging researchers can use the atlas for fine-grained automated segmentation (as shown below), or as a highly detailed CCF for population analyses.

Automated segmentation of ultra-high-resolution *ex vivo* MRI

One of the new analyses that *NextBrain* enables is the automated fine-grained segmentation of ultra-high-resolution *ex vivo* MRI. Since motion is not a factor in *ex vivo* imaging, very long MRI scanning times can be used to acquire data at resolutions that are infeasible *in vivo*. One example is the publicly available 100µm isotropic whole brain presented in [2], which was acquired in a 100-hour session on a 7T MRI scanner. Such datasets have huge potential in mesoscopic studies connecting microscopy with *in vivo* imaging [57].

Volumetric segmentation of ultra-high-resolution *ex vivo* MRI can be highly advantageous in neuroimaging in two different manners. First, by supplementing such scans (like the 100-micron brain) with neuroanatomical information that augments their value as atlases, e.g., as common coordinate frames or for segmentation purposes [58]. And second, by enabling analyses of *ex vivo* MRI datasets at scale (e.g., volumetry or shape analysis).

Dense manual segmentation of these datasets is practically infeasible, as it entails manually tracing ROIs on over 1,000 slices. Moreover, one typically seeks to label these images at a higher level of detail than *in vivo* (i.e., more ROIs of smaller sizes), which exacerbates the problem. One could utilise semi-automated methods like the AI-assisted technique we used in to build *NextBrain* (see previous section), which limits the manual segmentation to one every *N* slices [48] (*N=4* in this work). However, such a strategy only ameliorates the problem to a certain degree, as tedious manual segmentation is still required for a significant fraction of slices.

A more appealing alternative is automated segmentation. However, existing approaches have limitations, as they either: *(i)* were designed for 1mm *in vivo* scans and do not capitalise on the increased resolution of *ex vivo* MRI [54,59]; or *(ii)* utilise neural networks trained with *ex vivo* scans but with a limited number of ROIs, due to the immense labelling effort that is required to generate the training data [50].

This limitation is circumvented by *NextBrain*: as a probabilistic atlas of neuroanatomy, it can be combined with well-established Bayesian segmentation methods (which are adaptive to MRI contrast) to segment ultra-high-resolution *ex vivo* MRI scans into 333 ROIs. We have released in FreeSurfer an implementation that segments full brain scans in approximately 1h, using a desktop equipped with a graphics processing unit (GPU).

We applied this Bayesian tool to the public 100-micron brain [2]. Sample slices and their corresponding automated segmentations are shown in Fig. 4. The exquisite resolution and contrast of the dataset enables our atlas to accurately delineate a large number of ROIs with very different sizes, including small nuclei and subregions of the hippocampus, amygdala, thalamus, hypothalamus, midbrain, etc.

To the best of our knowledge, this is the most comprehensive dense segmentation of a human brain MRI scan to date. As *ex vivo* datasets with tens of scans become available [50,60,61], our tool has great potential in augmenting mesoscopic studies of the human brain.

Fine-grained anatomical signature of ageing

NextBrain can also be used to automatically segment *in vivo* MRI scans at the resolution of the atlas, i.e., 200µm isotropic. Scans used in research typically have isotropic

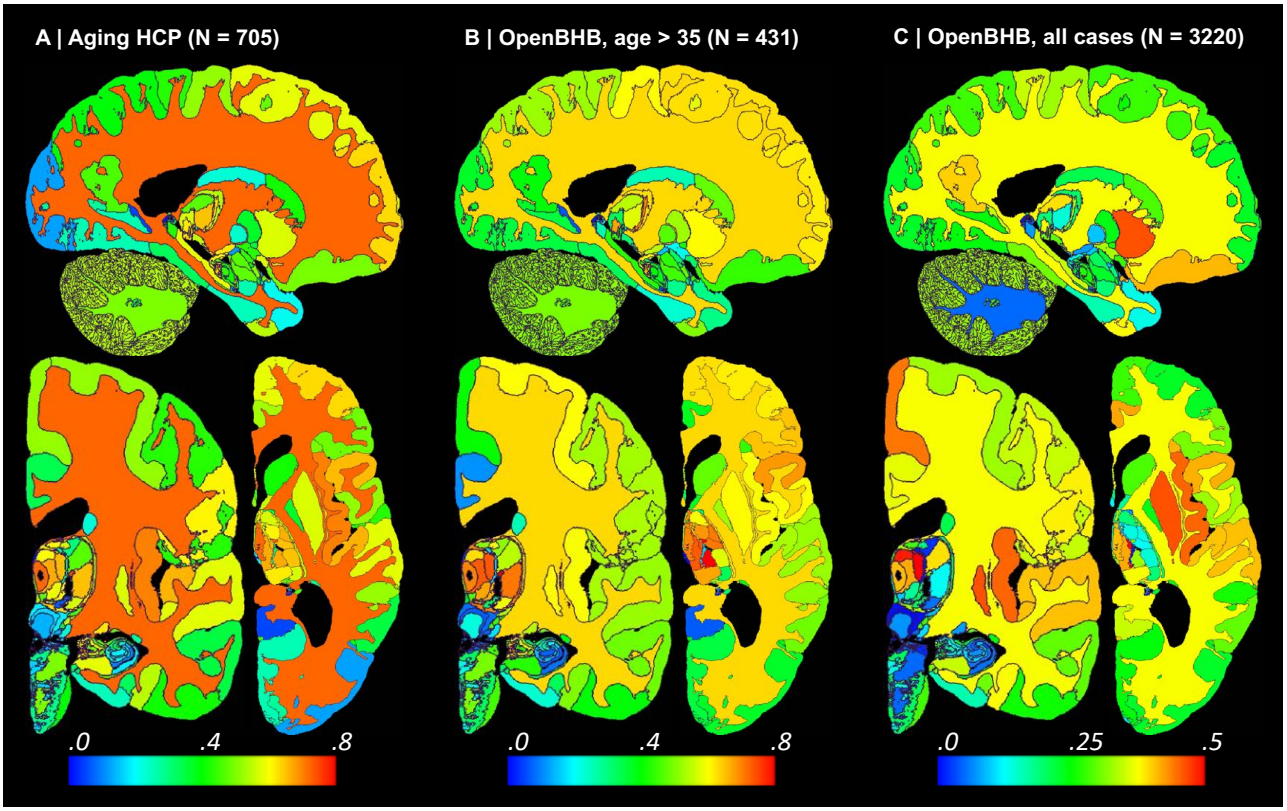

Fig. 5: Absolute value of Spearman correlation for ROI volumes vs age derived from in vivo MRI scans: (A) Ageing HCP dataset (image resolution: .8mm isotropic; age range: 36-90 years; mean age: 59.6 years). (B) OpenBHB dataset [1], restricted to subjects with age over 35 years to match Ageing HCP (image resolution 1mm isotropic; age range: 36-86 years; mean age: 57.9 years). (C) Full OpenBHB dataset (age range: 6-86 years, mean age: 25.2 years); please note the different scale of the colour bar. The ROI volumes are corrected by intracranial volume (by division) and sex (by regression). Further slices are shown in Extended Fig. 6.

resolution with voxel sizes ranging from 0.7 to 1.2mm, and therefore do not reveal all ROI boundaries with as much detail as ultra-high-resolution *ex vivo* MRI. However, many boundaries are still visible, including the external boundaries of brain structures (hippocampus, thalamus, etc.) and some internal boundaries, e.g., between the anteromedial and lateral posterior thalamus [62]. Bayesian segmentation capitalises on these visible boundaries and combines them with the prior knowledge encoded in the atlas to produce the full subdivision – albeit with lower reliability for the indistinct boundaries [40]. A sample segmentation is shown in Fig. 1F.

We first evaluated the *in vivo* segmentation quantitatively on OpenBHB [1], a public dataset that aggregates over 3,000 ~1mm isotropic T1-weighted scans of healthy individuals from 10 different studies and over 60 sites. Using FreeSurfer 7.0 as a silver standard, we computed Dice scores for our segmentations at the level of whole regions, i.e., the level of granularity provided by FreeSurfer. The Dice scores are shown in Extended Data Fig. 5, and they are in the range expected from Bayesian segmentation methods [54] – although slightly lower for the white matter structures (cerebellar and cerebral white matter, brainstem) due to the differences in anatomical definitions between the FreeSurfer atlas and *NextBrain* (particularly in the midbrain region).

We then performed Bayesian segmentation with *NextBrain* on 705 scans from the Ageing HCP dataset [63], aged 36-90 years (mean: 59.6 years). This is a high-quality *in vivo* dataset (0.8mm resolution) that enables fitting the atlas with higher accuracy. We computed the volumes of the ROIs for every subject, corrected them for total intracranial volume (by division) and sex (by regression), and computed their Spearman correlation with age. We used the Spearman rather than Pearson correlation because, being rank-based, it is a better model for ageing trajectories as they are known to be nonlinear for wide age ranges [64,65].

The result of this analysis is, to the best of our knowledge, the most comprehensive map of regional ageing of the human brain to date (Fig. 5A and Extended Data Fig. 6A). Cortically, we found significant negative correlations with age in the prefrontal cortex and insula, whilst the temporal and parahippocampal cortices did not yield significant correlation – which is consistent with findings from studies of cortical thickness [27,66]. The white matter is known to decline steadily after ~35 years [64,65], and such negative correlation is also detected by *NextBrain*. Other general ageing patterns at the whole structure level [64,65] are also successfully captured, such as a steady volume decrease of the caudate, thalamus, or putamen, or the volumetric reduction of the hippocampus, amygdala, or globus pallidus.

Importantly, *NextBrain* also unveils more granular patterns of the relationship between volumes and ageing within these regions. For example, the anterior caudate showed a stronger negative correlation between age and volume than the posterior caudate. Similarly, the external segment of the globus pallidus showed a stronger correlation than the internal segment. In the hippocampus, subicular regions correlate more strongly than the rest of the structure. In the thalamus, the correlation is more significant in the mediodorsal, anteroventral, and pulvinar nuclei. The pattern of correlation strength is more homogeneous across subregions in the amygdala, hypothalamus, and cerebellum.

We then revisited the OpenBHB dataset and performed the same regression analysis only for subjects older than 35 years, to match the age range of the Ageing HCP dataset (N=431, aged 36-86 years, mean 57.9 years). The results are shown in Fig. 5B and Extended Data Fig. 6B. Despite the differences in acquisition and the huge heterogeneity of the OpenBHB dataset, the results are highly consistent with those from HCP – but with slightly lower significance, possibly due to the increased voxel size (twice as big, since $1/0.8^3 \approx 2$).

We also performed the same analysis with all 3,220 subjects in OpenBHB; see results in Fig. 5C and Extended Data Fig. 6C. For many regions, widening the age range to 6-86 years (mean age: 25.2) yields non-monotonic ageing curves and therefore weaker Spearman correlations. Therefore, these graphs highlight the regions whose volumes start decreasing with age the earliest, such as the putamen or medial thalamus. Many other patterns of association between age and ROI volumes remain very similar to those of the older populations (e.g., basal ganglia or hippocampus).

The segmentation code is publicly available in FreeSurfer: https://surfer.nmr.mgh.harvard.edu/fswiki/HistoAtlasSegmentation and can be run with a single line of code. This enables researchers worldwide to analyse their scans at a superior level of detail without manual effort or highly specific neuroanatomical knowledge.

Discussion and Conclusion

NextBrain is a next-generation probabilistic human brain atlas, which is publicly available and distributed with a companion Bayesian segmentation tool and multi-modal dataset. The dataset itself is already a highly valuable resource: researchers have free access to both the raw and registered data, which they can use for their own research (e.g., in MRI signal modelling or registration), or to augment the atlas with new ROIs, e.g., by labelling them on the histology or MRI data and rebuilding the atlas. The atlas itself is a novel, high-resolution common coordinate frame for population analyses. The Bayesian tool enables segmentation of *ex vivo* and *in vivo* MRI at an unprecedented level of granularity.

Due to its volumetric and semantic nature, NextBrain can be complemented by other segmentation methods and atlases that describe other aspects of the brain. For example, more accurate cortical segmentation and parcellation can be achieved with surface models [67]. We are currently working on models that combine neural networks with geometry processing to obtain laminar segmentations from both *in vivo* and *ex vivo* scans [68,69]. Surface placement will also warrant compatibility with cortical atlases obtained with multimodal data [37].

NextBrain is compatible with 1mm isotropic scans, but is particularly useful in analysing datasets with higher resolution – both *in vivo* and *ex vivo*, including ultra-high field MRI (e.g., 7T) and exciting new modalities like HiP-CT [70]. As such high-resolution data become increasingly available, the ability to analyse them with superior granularity using *NextBrain* holds great promise to advance knowledge about the human brain in health and in disease.

Methods

Brain specimens

Hemispheres from five individuals (including half of the cerebrum, cerebellum, and brainstem), were used in this study, following informed consent to use the tissue for research and the ethical approval for research by the National Research Ethics Service (NRES) Committee London-Central. All hemispheres were fixed in 10% neutral buffered formalin (Fig. 1A). The laterality and demographics are summarised in Table 1 below; the donors were neurologically normal, but one case had an undiagnosed, asymptomatic tumour (diameter: ~10mm) in the white matter, adjacent to the pars opercularis. This tumour did not pose issues in any of the processing steps described below.

Table 1 Demographics of the five cases used in this study.

Case	Age at death	Sex	Laterality	Incidental findings
Case 1	94 years	Female	Right	None
Case 2	84 years	Female	Right	None
Case 3	80 years	Male	Right	None
Case 4	79 years	Female	Left	Tumour adjacent to pars opercularis
Case 5	78 years	Male	Left	None

Data acquisition

Our data acquisition pipeline largely leverages our previous work [47]. We summarise it here for completeness; the reader is referred to the corresponding publication for further details.

- *MRI scanning.* Prior to dissection, the hemispheres were scanned on a 3T Siemens MAGNETOM Prisma scanner. The specimens were placed in a container filled

with Fluorinert (perfluorocarbon), a proton-free fluid with no MRI signal that yields excellent *ex vivo* MRI contrast and does not affect downstream histological analysis [71]. The MRI scans were acquired with a T2-weighted sequence (optimised long echo train 3D fast spin echo [72]) with parameters: TR = 500 ms, TEeff = 69ms, BW = 558 Hz/Px, echo spacing = 4.96ms, echo train length = 58, 10 averages, with 400µm isotropic resolution, acquisition time for each average = 547s, total scanning time = 91 min. These scans were processed with a combination of SAMSEG [54] and the FreeSurfer 7.0 cortical stream [67] to bias field correct the images, generate rough subcortical segmentations, and obtain white matter and pial surfaces with corresponding parcellations according to the Desikan-Killiany atlas [49] (Fig. 1B).

- *Dissection.* After MRI scanning, each hemisphere is dissected to fit into standard 74x52mm cassettes. First, each hemisphere was split into cerebrum, cerebellum, and brainstem. Using a metal frame as a guide, these were subsequently cut into 10mm-thick slices in coronal, sagittal, and axial orientation, respectively. These slices were photographed inside a rectangular frame of known dimensions for pixel size and perspective correction; we refer to these images as "whole slice photographs." While the brainstem and cerebellum slices all fit into the cassettes, the cerebrum slices were further cut into as many blocks as needed. "Blocked slice photographs" were also taken for these blocks (Fig. 1C, left).

- *Tissue processing and sectioning.* After standard tissue processing steps, each tissue block was embedded in paraffin wax and sectioned with a sledge microtome at 25μm thickness. Before each cut, a photograph was taken with a 24MPx Nikon D5100 camera (ISO = 100, aperture = f/20, shutter speed = automatic) mounted right above the microtome, pointed perpendicularly to the sectioning plane. These photographs (henceforth "blockface photographs") were corrected for pixel size and perspective using fiducial markers. The blockface photographs have poor contrast between grey and white matter (Fig. 1C, right) but also negligible nonlinear geometric distortion, so they can be readily stacked into 3D volumes. A 2D convolutional neural network (CNN) pretrained on the ImageNet dataset [73] and fine-tuned on 50 manually labelled examples was used to automatically produce binary tissue masks for the blockface images.

- *Staining and digitisation.* We mounted on glass slides and stained two consecutive sections every *N* (see below), one with Hematoxylin and Eosin (H&E) and one with Luxol Fast Blue (LFB); see Fig. 1D. The sampling interval was *N=10* (i.e., 250μm) for blocks that included subcortical structures in the cerebrum, medial structures of the cerebellum, or brainstem structures. The interval was *N=20* (500μm) for all other blocks. All stained sections were digitised with a flatbed scanner at 6,400 DPI resolution (pixel size: 3.97μm). Tissue masks were generated using a 2D CNN similar to the one used for blockface photographs (pretrained on ImageNet and finetuned on 100 manually labelled examples).

Dense labelling of histology

Segmentations of 333 ROIs (34 cortical, 299 subcortical) were made by authors ER, JA, and EB (with guidance from DK, MB, JZ, and JCA) for all the LFB sections, using a combination of manual and automated techniques (Fig. 1E). The general procedure to label each block was: *(i)* produce an accurate segmentation for one of every four sections; *(ii)* run SmartInterpol [48] to automatically segment the sections in between; and *(iii)* manually correct these automatically segmented sections when needed. SmartInterpol is a dedicated AI technique that we have developed specifically to speed up segmentation of histological stacks in this project.

To obtain accurate segmentations on sparse sections, we used two different strategies depending on the brain region. For the blocks containing subcortical or brainstem structures, ROIs were manually traced from scratch using a combination of ITK-SNAP [74] and FreeSurfer's viewer "Freeview". For cerebellum blocks, we first trained a 2D CNN (a U-Net [75]) on 20 sections on which we had manually labelled the white matter and the molecular and granular layers of the cortex. The CNN was then run on the (sparse) sections, and the outputs manually corrected. This procedure saves a substantial amount of time, since manually tracing the convoluted shape of the arbor vitae is extremely time consuming. For the cortical cerebrum blocks, we used a similar strategy as for the cerebellum, labelling the tissue as either white or grey matter. The subdivision of the cortical grey matter into parcels was achieved by taking the nearest neighbouring cortical label from the aligned MRI scan (details on the alignment below).

The manual labelling followed neuroanatomical protocols based on different brain atlases, depending on the brain region. Further details on the specific delineation protocols are provided in the Supplementary Methods. The general ontology of the 333 ROIs is based on the Allen reference brain [3], and is provide in a spreadsheet as part of the Supplementary Data.

3D histology reconstruction

3D histology reconstruction is the inverse problem of reversing all the distortion that brain tissue undergoes during acquisition, in order to reassemble a 3D shape that accurately follows the original anatomy. For this purpose, we used a framework with four modules.

- *Initial blockface alignment.* In order to roughly initialise the 3D reconstruction, we relied on the stacks of blockface photographs. Specifically, we used our previously presented hierarchical joint registration framework [44]

that seeks to: *(i)* align each block to the MRI with a similarity transform, by maximising the normalised cross-correlation of their intensities; while *(ii)* discouraging overlap between blocks or gaps in between, via a differentiable regulariser. The similarity transforms allowed for rigid deformation (rotation, translation), as well as isotropic scaling to model the shrinking due to tissue processing. The registration algorithm was initialised with transforms derived from the whole slice, blocked slice, and blockface photographs (see details in [47]). The registration was hierarchical in the sense that groups of transforms were forced to share the same parameters in the earlier iterations of the optimisation, to reflect our knowledge of the cutting procedure. In the first iterations, we clustered the blocks into three groups: cerebrum, cerebellum, and brainstem. In the following iterations, we clustered the cerebral blocks that were cut from the same slice, and allowed translations in all directions, in-plane rotation, and global scaling. In the final iterations, each block alignment was optimised independently. The numerical optimisation used the LBFGS algorithm [76]. The approximate average error after this procedure was ~2mm [44]. A sample 3D reconstruction is shown in Fig. 1F.

- *Refined alignment with preliminary nonlinear model.* Once a good initial alignment is available, we can use the LFB sections to refine the registration. These LFB images have exquisite contrast (Fig. 1D) but suffer from nonlinear distortion – rendering the good initialization from the blockface images crucial. The registration procedure was nearly identical to that of the blockface, with two main differences. First, the similarity term used the local (rather than global) normalised cross-correlation function [77] in order to handle uneven staining across sections. Second, the deformation model and optimisation hierarchy were slightly different since nonlinear registration benefits from more robust methods. Specifically: The first two levels of optimisation were the same, with blocks grouped into cerebrum/cerebellum/brainstem (first level) or cerebral slices (second level), and optimisation of similarity transforms. The third level (i.e., each block independently) was subdivided into four stages in which we optimised transforms with increasing complexity: *(i)* we allowed for translations in all directions, in-plane rotation and global scaling (5 parameters); *(ii)* we added a different scaling parameter in the normal direction of the block (6 parameters); *(iii)* we allowed for rotation in all directions (8 parameters); and *(iv)* we added a nonlinear field modelled with a grid of control points (10mm spacing) and interpolating B-splines.

- *Nonlinear AI registration.* We seek to produce final nonlinear registrations that are accurate, consistent with each other, and robust against tears and folds in the sections. We capitalise on Synth-by-Reg (SbR [45]), an AI tool for multimodal registration that we have recently developed, to register histological sections to MRI slices resampled to the plane of the histology (as estimated by the linear alignment). SbR exploits the facts that: *(i)* intra-modality registration is more accurate than inter-modality registration [78]; and *(ii)* there is a correspondence between histological sections and MRI slices, i.e., they represent the same anatomy. In short, SbR trains a CNN to make histological sections look like MRI slices (a task known as style transfer [79]), using a second CNN that has been previously trained to register MRI slices to each other. The style transfer relies on the fact that only good MRI synthesis will yield a good match when used as input to the second CNN, combined with a contrastive loss [80] that prevents blurring and content shift due to overfitting. SbR produces highly accurate deformations parameterized as stationary velocity fields (SVF [81]).

- *Bayesian refinement.* Running SbR for each stain and section independently (i.e., LFB to resampled MRI, and H&E to resampled MRI) yields a reconstruction that is jagged and sensitive to folds and tears. One alternative is to register each histological section to each neighbour directly, which achieves smooth reconstructions but incurs the so-called "banana effect", i.e., a straightening of curved structures [42]. We have proposed a Bayesian method that yields smooth reconstructions without banana effect [46]. This method follows an overconstrained strategy, by computing registrations between: LFB and MRI; H&E and MRI; H&E and LFB; each LFB section and the two nearest neighbours in either direction across the stack; each H&E section and its neighbours; and each MRI slice and its neighbours. For a stack with *S* sections, this procedure yields 15*xS-18* registrations, while the underlying dimensionality of the spanning tree connecting all the images is just 3xS-1. We use a probabilistic model of SVFs to infer the most likely spanning tree given the computed registrations, which are seen as noisy measurements of combinations of transforms in the spanning tree. The probabilistic model uses a Laplace distribution, which relies on L1 norms and is thus robust to outliers. Moreover, the properties of SVFs enable us to write the optimization problem as a linear program, which we solve with a standard simplex algorithm [82]. The result of this procedure was a 3D reconstruction that is accurate (it is informed by many registrations), robust, and smooth (Figures 1G and 2).

Atlas construction

The transforms for the LFB sections produced by the 3D reconstructions were applied to the segmentations to bring them into 3D space. Despite the regulariser from [44], minor overlaps and gaps between blocks still occur. The former were resolved by selecting the label which is furthest inside the corresponding ROI. For the latter, we used our previously developed smoothing approach [62].

Given the low number of available cases, we combined the left (2) and right (3) hemispheres into a single atlas. This was achieved by flipping the right hemispheres and computing a probabilistic atlas of the left hemisphere using an unbiased technique [53]. To initialise the procedure, we registered the MRI scans to the MNI atlas [83] with the right hemisphere masked out, and averaged the deformed segmentations to obtain an initial estimate of the probabilistic atlas. From that point on, the algorithm operates exclusively on the segmentations.

Every iteration of the atlas construction process comprises two steps. First, the current estimate of the atlas and the segmentations are co-registered one at the time, using: *(i)* a diffeomorphic deformation model based on SVFs parameterized by grids of control points and B-splines (as implemented in NiftyReg [84]), which preserves the topology of the segmentations; *(ii)* a data term, which is the log-likelihood of the label at each voxel according to the probabilities given by the deformed atlas (with a weak Dirichlet prior to prevent logs of zero); and *(iii)* a regulariser based on the bending energy of the field, which encourages regularity in the deformations. The second step of each iteration updates the atlas by averaging the segmentations. The procedure converged (negligible change in the atlas) after five iterations. Slices of the atlas are shown in Figs. 1H and 3.

Bayesian segmentation

Our Bayesian segmentation algorithm builds on well-established methods in the neuroimaging literature [59,85,86]. In short, the algorithm jointly estimates a set of parameters that best explain the observed image in light of the probabilistic atlas, according to a generative model based on a Gaussian mixture model (GMM) conditioned on the segmentation, combined with a model of bias field. The parameters include the deformation of the probabilistic atlas, a set of coefficients describing the bias field, and the means, variances, and weights of the GMM. The atlas deformation is regularised in the same way as the atlas construction (bending energy, in our case) and is estimated via numerical optimisation with LBFGS. The bias field and GMM parameters are estimated with the Expectation Maximisation algorithm [87].

Compared with classical Bayesian segmentation methods operating at 1mm resolution with just a few classes (e.g., SAMSEG [54], SPM [59]), our proposed method has several distinct features:

- Since the atlas only describes the left hemisphere, we use a fast deep learning registration method (EasyReg [88]) to register the input scan to MNI space, and use the resulting deformation to split the brain into two hemispheres that are processed independently.
- Since the atlas only models brain tissue, we run SynthSeg [89] on the input scan to mask out the extracerebral tissue.
- Clustering ROIs into tissue types (rather than letting each ROI have its own Gaussian) is particularly important, given the large number of ROIs (333). The user can specify the clustering via a configuration file; by default, our public implementation uses a configuration with 15 tissue types, tailored to *in vivo* MRI segmentation.
- The framework is implemented using the PyTorch package, which enables it to run on GPUs and curbs segmentation run times to about half an hour per hemisphere.

Sample segmentations with this method can be found in Figures 1H (*in vivo*) and 4 (*ex vivo*).

Acknowledgements

The authors would like to thank the donors, without whom this work would have not been possible. The authors would also like to acknowledge Dr. Paul Johns for his invaluable courses in neuroanatomy at St George's, University of London.

Author contributions

- *Conceptualization:* JCA, BLE, JLH, ZJ, JEI
- *Data curation:* AC, MM, ER, JA, SC, EB, BB, AA, LZ, DLT, DK, MB
- *Formal analysis:* AC, LZ, JEI
- *Funding acquisition:* JEI
- *Investigation:* AC, MM, ER, LP, RA, JA, SC, EB, LZ, JEI
- *Methodology:* AC, MM, OP, YB, JLH, ZJ, JEI
- *Project administration:* ER, JLH, CS, ZJ, JEI
- *Resources:* DLT, JLH, CS, ZJ
- *Software:* AC, MM, BB, AA, OP, YB, PS, JH, JEI
- *Supervision:* ER, LP, DK, MB, JLH, CS, ZJ, JEI
- *Validation:* AC, JEI
- *Visualisation:* AC, PS, JH, JEI
- *Writing – original draft:* AC, ER, JEI
- *Writing – review & editing:* all authors.

Funding

This research has been primarily funded by the European Research Council awarded to JEI (Starting Grant 677697, project “BUNGEE-TOOLS”). MB is supported by a Fellowship award from the Alzheimer’s Society, UK (AS-JF-19a-004-517). OP is supported by a grant from the Lundbeck foundation (R360–2021–39). MM is supported by the Italian National Institute of Health with a Starting Grant, and by the Wellcome Trust through a Sir Henry Wellcome Fellowship (213722/Z/18/Z).

Data availability

The raw data used in this article (MRI, histology, delineations, etc.) can be downloaded from: https://doi.org/10.5522/04/24243835

An online tool to interactively explore the 3D reconstructed data can be found here: https://github-pages.ucl.ac.uk/NextBrain

Code availability

The code used in this article for 3D histology reconstruction can be downloaded from: https://github.com/acasamitjana/ERC_reconstruction and used and distributed freely.

The segmentation tool is provided as Python code and is integrated in our neuroimaging toolkit "FreeSurfer": https://surfer.nmr.mgh.harvard.edu/fswiki/HistoAtlas-Segmentation. The source code is available on GitHub: https://github.com/freesurfer/free-surfer/tree/dev/mri_histo_util

Competing interests

The authors have no relevant financial or non-financial interests to disclose.

References

1 Dufumier, B. *et al.* OpenBHB: a Large-Scale Multi-Site Brain MRI Data-set for Age Prediction and Debiasing. *NeuroImage* **263**, 119637 (2022).

2 Edlow, B. L. *et al.* 7 Tesla MRI of the ex vivo human brain at 100 micron resolution. *Scientific data* **6**, 244 (2019).

3 Ding, S. L. *et al.* Comprehensive cellular-resolution atlas of the adult human brain. *Journal of comparative neurology* **524**, 3127-3481 (2016).

4 Amunts, K. *et al.* BigBrain: an ultrahigh-resolution 3D human brain model. *Science* **340**, 1472-1475 (2013).

5 Amunts, K., Mohlberg, H., Bludau, S. & Zilles, K. Julich-Brain: A 3D probabilistic atlas of the human brain's cytoarchitecture. *Science* **369**, 988-992 (2020).

6 Yacoub, E. *et al.* Imaging brain function in humans at 7 Tesla. *Magnetic Resonance in Medicine: An Official Journal of the International Society for Magnetic Resonance in Medicine* **45**, 588-594 (2001).

7 Griswold, M. A. *et al.* Generalized autocalibrating partially parallel acquisitions (GRAPPA). *Magnetic Resonance in Medicine: An Official Journal of the International Society for Magnetic Resonance in Medicine* **47**, 1202-1210 (2002).

8 Pruessmann, K. P., Weiger, M., Scheidegger, M. B. & Boesiger, P. SENSE: sensitivity encoding for fast MRI. *Magnetic Resonance in Medicine: An Official Journal of the International Society for Magnetic Resonance in Medicine* **42**, 952-962 (1999).

9 Keil, B. *et al.* A 64-channel 3T array coil for accelerated brain MRI. *Magnetic resonance in medicine* **70**, 248-258 (2013).

10 Maclaren, J., Herbst, M., Speck, O. & Zaitsev, M. Prospective motion correction in brain imaging: a review. *Magnetic resonance in medicine* **69**, 621-636 (2013).

11 Bernstein, M. A., King, K. F. & Zhou, X. J. *Handbook of MRI pulse sequences*. (Elsevier, 2004).

12 Ogawa, S., Lee, T.-M., Kay, A. R. & Tank, D. W. Brain magnetic resonance imaging with contrast dependent on blood oxygenation. *proceedings of the National Academy of Sciences* **87**, 9868-9872 (1990).

13 Cha, S. *et al.* Intracranial mass lesions: dynamic contrast-enhanced susceptibility-weighted echo-planar perfusion MR imaging. *Radiology* **223**, 11-29 (2002).

14 Paldino, M. J. & Barboriak, D. P. Fundamentals of quantitative dynamic contrast-enhanced MR imaging. *Magnetic resonance imaging clinics of North America* **17**, 277-289 (2009).

15 Kwong, K. K. *et al.* MR perfusion studies with T1-weighted echo planar imaging. *Magnetic Resonance in Medicine* **34**, 878-887 (1995).

16 Reichenbach, J. R., Venkatesan, R., Schillinger, D. J., Kido, D. K. & Haacke, E. M. Small vessels in the human brain: MR venography with deoxyhemoglobin as an intrinsic contrast agent. *Radiology* **204**, 272-277 (1997).

17 Basser, P. J., Mattiello, J. & LeBihan, D. MR diffusion tensor spectroscopy and imaging. *Biophysical journal* **66**, 259-267 (1994).

18 Le Bihan, D. *et al.* Diffusion tensor imaging: concepts and applications. *Journal of Magnetic Resonance Imaging: An Official Journal of the International Society for Magnetic Resonance in Medicine* **13**, 534-546 (2001).

19 Fischl, B. FreeSurfer. *Neuroimage* **62**, 774-781 (2012).

20 Smith, S. M. *et al.* Advances in functional and structural MR image analysis and implementation as FSL. *Neuroimage* **23**, S208-S219 (2004).

21 Penny, W. D., Friston, K. J., Ashburner, J. T., Kiebel, S. J. & Nichols, T. E. *Statistical parametric mapping: the analysis of functional brain images*. (Elsevier, 2011).

22 Cox, R. W. AFNI: software for analysis and visualization of functional magnetic resonance neuroimages. *Computers and Biomedical research* **29**, 162-173 (1996).

23 Hibar, D. P. *et al.* Common genetic variants influence human subcortical brain structures. *Nature* **520**, 224-229 (2015).

24 Thompson, P. M. *et al.* ENIGMA and global neuroscience: A decade of large-scale studies of the brain in health and disease across more than 40 countries. *Translational psychiatry* **10**, 100 (2020).

25 Dima, D. *et al.* Subcortical volumes across the lifespan: Data from 18,605 healthy individuals aged 3–90 years. *Human brain mapping* **43**, 452-469 (2022).

26 Frangou, S. *et al.* Cortical thickness across the lifespan: Data from 17,075 healthy individuals aged 3–90 years. *Human brain mapping* **43**, 431-451 (2022).
27 Salat, D. H. *et al.* Thinning of the cerebral cortex in aging. *Cerebral cortex* **14**, 721-730 (2004).
28 Ingalhalikar, M. *et al.* Sex differences in the structural connectome of the human brain. *Proceedings of the National Academy of Sciences* **111**, 823-828 (2014).
29 McDonald, C. *et al.* Regional rates of neocortical atrophy from normal aging to early Alzheimer disease. *Neurology* **73**, 457-465 (2009).
30 Agosta, F. *et al.* White matter damage in Alzheimer disease and its relationship to gray matter atrophy. *Radiology* **258**, 853-863 (2011).
31 Jack Jr, C. R. *et al.* The Alzheimer's disease neuroimaging initiative (ADNI): MRI methods. *Journal of Magnetic Resonance Imaging: An Official Journal of the International Society for Magnetic Resonance in Medicine* **27**, 685-691 (2008).
32 Van Essen, D. C. *et al.* The WU-Minn human connectome project: an overview. *Neuroimage* **80**, 62-79 (2013).
33 Ge, J. *et al.* Increasing diversity in connectomics with the Chinese Human Connectome Project. *Nature Neuroscience* **26**, 163-172 (2023).
34 Alfaro-Almagro, F. *et al.* Image processing and Quality Control for the first 10,000 brain imaging datasets from UK Biobank. *Neuroimage* **166**, 400-424 (2018).
35 Fonov, V. *et al.* Unbiased average age-appropriate atlases for pediatric studies. *Neuroimage* **54**, 313-327 (2011).
36 Fischl, B. *et al.* Whole brain segmentation: automated labeling of neuroanatomical structures in the human brain. *Neuron* **33**, 341-355 (2002).
37 Glasser, M. F. *et al.* A multi-modal parcellation of human cerebral cortex. *Nature* **536**, 171-178 (2016).
38 Rolls, E. T. A computational theory of episodic memory formation in the hippocampus. *Behavioural brain research* **215**, 180-196 (2010).
39 Yushkevich, P. A. *et al.* A high-resolution computational atlas of the human hippocampus from postmortem magnetic resonance imaging at 9.4 T. *Neuroimage* **44**, 385-398 (2009).
40 Iglesias, J. E. *et al.* A computational atlas of the hippocampal formation using ex vivo, ultra-high resolution MRI: application to adaptive segmentation of in vivo MRI. *Neuroimage* **115**, 117-137 (2015).
41 Saygin, Z. M. *et al.* High-resolution magnetic resonance imaging reveals nuclei of the human amygdala: manual segmentation to automatic atlas. *Neuroimage* **155**, 370-382 (2017).
42 Pichat, J., Iglesias, J. E., Yousry, T., Ourselin, S. & Modat, M. A survey of methods for 3D histology reconstruction. *Medical image analysis* **46**, 73-105 (2018).
43 Alkemade, A. *et al.* A unified 3D map of microscopic architecture and MRI of the human brain. *Science advances* **8**, eabj7892 (2022).
44 Mancini, M. *et al.* in *2019 IEEE 16th International Symposium on Biomedical Imaging (ISBI 2019).* 666-669 (IEEE).
45 Casamitjana, A., Mancini, M. & Iglesias, J. E. in *Simulation and Synthesis in Medical Imaging: 6th International Workshop, SASHIMI 2021, Held in Conjunction with MICCAI 2021, Strasbourg, France, September 27, 2021, Proceedings 6.* 44-54 (Springer).
46 Casamitjana, A. *et al.* Robust joint registration of multiple stains and MRI for multimodal 3D histology reconstruction: Application to the Allen human brain atlas. *Medical image analysis* **75**, 102265 (2022).
47 Mancini, M. *et al.* A multimodal computational pipeline for 3D histology of the human brain. *Scientific reports* **10**, 13839 (2020).
48 Atzeni, A., Jansen, M., Ourselin, S. & Iglesias, J. E. in *Medical Image Computing and Computer Assisted Intervention–MICCAI 2018: 21st International Conference, Granada, Spain, September 16-20, 2018, Proceedings, Part II 11.* 219-227 (Springer).
49 Desikan, R. S. *et al.* An automated labeling system for subdividing the human cerebral cortex on MRI scans into gyral based regions of interest. *Neuroimage* **31**, 968-980 (2006).
50 Khandelwal, P. *et al.* Automated deep learning segmentation of high-resolution 7 T ex vivo MRI for quantitative analysis of structure-pathology correlations in neurodegenerative diseases. *arXiv preprint arXiv:2303.12237* (2023).
51 Salehi, P. & Chalechale, A. in *2020 International Conference on Machine Vision and Image Processing (MVIP).* 1-7 (IEEE).
52 Alyami, W., Kyme, A. & Bourne, R. Histological validation of MRI: A review of challenges in registration of imaging and whole-mount histopathology. *Journal of Magnetic Resonance Imaging* **55**, 11-22 (2022).
53 Joshi, S., Davis, B., Jomier, M. & Gerig, G. Unbiased diffeomorphic atlas construction for computational anatomy. *NeuroImage* **23**, S151-S160 (2004).
54 Puonti, O., Iglesias, J. E. & Van Leemput, K. Fast and sequence-adaptive whole-brain segmentation using parametric Bayesian modeling. *NeuroImage* **143**, 235-249 (2016).
55 Krauth, A. *et al.* A mean three-dimensional atlas of the human thalamus: generation from multiple histological data. *Neuroimage* **49**, 2053-2062 (2010).
56 Yelnik, J. *et al.* A three-dimensional, histological and deformable atlas of the human basal ganglia. I. Atlas construction based on immunohistochemical and MRI data. *Neuroimage* **34**, 618-638 (2007).
57 DeFelipe, J. From the connectome to the synaptome: an epic love story. *science* **330**, 1198-1201 (2010).
58 Horn, A. *et al.* Lead-DBS v2: Towards a comprehensive pipeline for deep brain stimulation imaging. *Neuroimage* **184**, 293-316 (2019).
59 Ashburner, J. & Friston, K. J. Unified segmentation. *Neuroimage* **26**, 839-851 (2005).

60 Costantini, I. *et al.* A cellular resolution atlas of Broca's area. *Science Advances* **9**, eadg3844 (2023).

61 https://dandiarchive.org/dandiset/000026.

62 Iglesias, J. E. *et al.* A probabilistic atlas of the human thalamic nuclei combining ex vivo MRI and histology. *Neuroimage* **183**, 314-326 (2018).

63 Bookheimer, S. Y. *et al.* The lifespan human connectome project in aging: an overview. *Neuroimage* **185**, 335-348 (2019).

64 Coupé, P., Catheline, G., Lanuza, E., Manjón, J. V. & Initiative, A. s. D. N. Towards a unified analysis of brain maturation and aging across the entire lifespan: A MRI analysis. *Human brain mapping* **38**, 5501-5518 (2017).

65 Billot, B. *et al.* Robust machine learning segmentation for large-scale analysis of heterogeneous clinical brain MRI datasets. *Proceedings of the National Academy of Sciences* **120**, e2216399120 (2023).

66 Llamas-Rodríguez, J. *et al.* TDP-43 and tau concurrence in the entorhinal subfields in primary age-related tauopathy and preclinical Alzheimer's disease. *Brain Pathology*, e13159 (2023).

67 Fischl, B. & Dale, A. M. Measuring the thickness of the human cerebral cortex from magnetic resonance images. *Proceedings of the National Academy of Sciences* **97**, 11050-11055 (2000).

68 Gopinath, K. *et al.* in *Medical Image Computing and Computer Assisted Intervention – MICCAI 2023.* (eds Hayit Greenspan *et al.*) 35-45 (Springer Nature Switzerland).

69 Zeng, X. *et al.* Segmentation of supragranular and infragranular layers in ultra-high resolution 7T ex vivo MRI of the human cerebral cortex. *bioRxiv*, 2023.2012.2006.570416 (2023).

70 Walsh, C. *et al.* Imaging intact human organs with local resolution of cellular structures using hierarchical phase-contrast tomography. *Nature methods* **18**, 1532-1541 (2021).

71 Iglesias, J. E. *et al.* Effect of fluorinert on the histological properties of formalin-fixed human brain tissue. *Journal of Neuropathology & Experimental Neurology* **77**, 1085-1090 (2018).

72 Mugler III, J. P. Optimized three-dimensional fast-spin-echo MRI. *Journal of magnetic resonance imaging* **39**, 745-767 (2014).

73 Simonyan, K. & Zisserman, A. Very deep convolutional networks for large-scale image recognition. *arXiv preprint arXiv:1409.1556* (2014).

74 Yushkevich, P. A. *et al.* User-guided 3D active contour segmentation of anatomical structures: significantly improved efficiency and reliability. *Neuroimage* **31**, 1116-1128 (2006).

75 Ronneberger, O., Fischer, P. & Brox, T. in *International Conference on Medical image computing and computer-assisted intervention.* 234-241 (Springer).

76 Liu, D. C. & Nocedal, J. On the limited memory BFGS method for large scale optimization. *Mathematical programming* **45**, 503-528 (1989).

77 Avants, B. B., Epstein, C. L., Grossman, M. & Gee, J. C. Symmetric diffeomorphic image registration with cross-correlation: evaluating automated labeling of elderly and neurodegenerative brain. *Medical image analysis* **12**, 26-41 (2008).

78 Iglesias, J. E. *et al.* in *International Conference on Medical Image Computing and Computer-Assisted Intervention.* 631-638 (Springer).

79 Jing, Y. *et al.* Neural style transfer: A review. *IEEE transactions on visualization and computer graphics* **26**, 3365-3385 (2019).

80 Chen, T., Kornblith, S., Norouzi, M. & Hinton, G. in *International conference on machine learning.* 1597-1607 (PMLR).

81 Arsigny, V., Commowick, O., Pennec, X. & Ayache, N. in *Medical Image Computing and Computer-Assisted Intervention–MICCAI 2006: 9th International Conference, Copenhagen, Denmark, October 1-6, 2006. Proceedings, Part I 9.* 924-931 (Springer).

82 Boyd, S. P. & Vandenberghe, L. *Convex optimization*. (Cambridge university press, 2004).

83 Mazziotta, J. *et al.* A probabilistic atlas and reference system for the human brain: International Consortium for Brain Mapping (ICBM). *Philosophical Transactions of the Royal Society of London. Series B: Biological Sciences* **356**, 1293-1322 (2001).

84 Modat, M. *et al.* Fast free-form deformation using graphics processing units. *Computer methods and programs in biomedicine* **98**, 278-284 (2010).

85 Van Leemput, K., Maes, F., Vandermeulen, D. & Suetens, P. Automated model-based tissue classification of MR images of the brain. *IEEE transactions on medical imaging* **18**, 897-908 (1999).

86 Wells, W. M., Grimson, W. E. L., Kikinis, R. & Jolesz, F. A. Adaptive segmentation of MRI data. *IEEE transactions on medical imaging* **15**, 429-442 (1996).

87 Dempster, A. P., Laird, N. M. & Rubin, D. B. Maximum likelihood from incomplete data via the EM algorithm. *Journal of the royal statistical society: series B (methodological)* **39**, 1-22 (1977).

88 Iglesias, J. E. A ready-to-use machine learning tool for symmetric multi-modality registration of brain MRI. *Scientific Reports* **13**, 6657 (2023).

89 Billot, B. *et al.* SynthSeg: Segmentation of brain MRI scans of any contrast and resolution without retraining. *Medical image analysis* **86**, 102789 (2023).

Extended Data

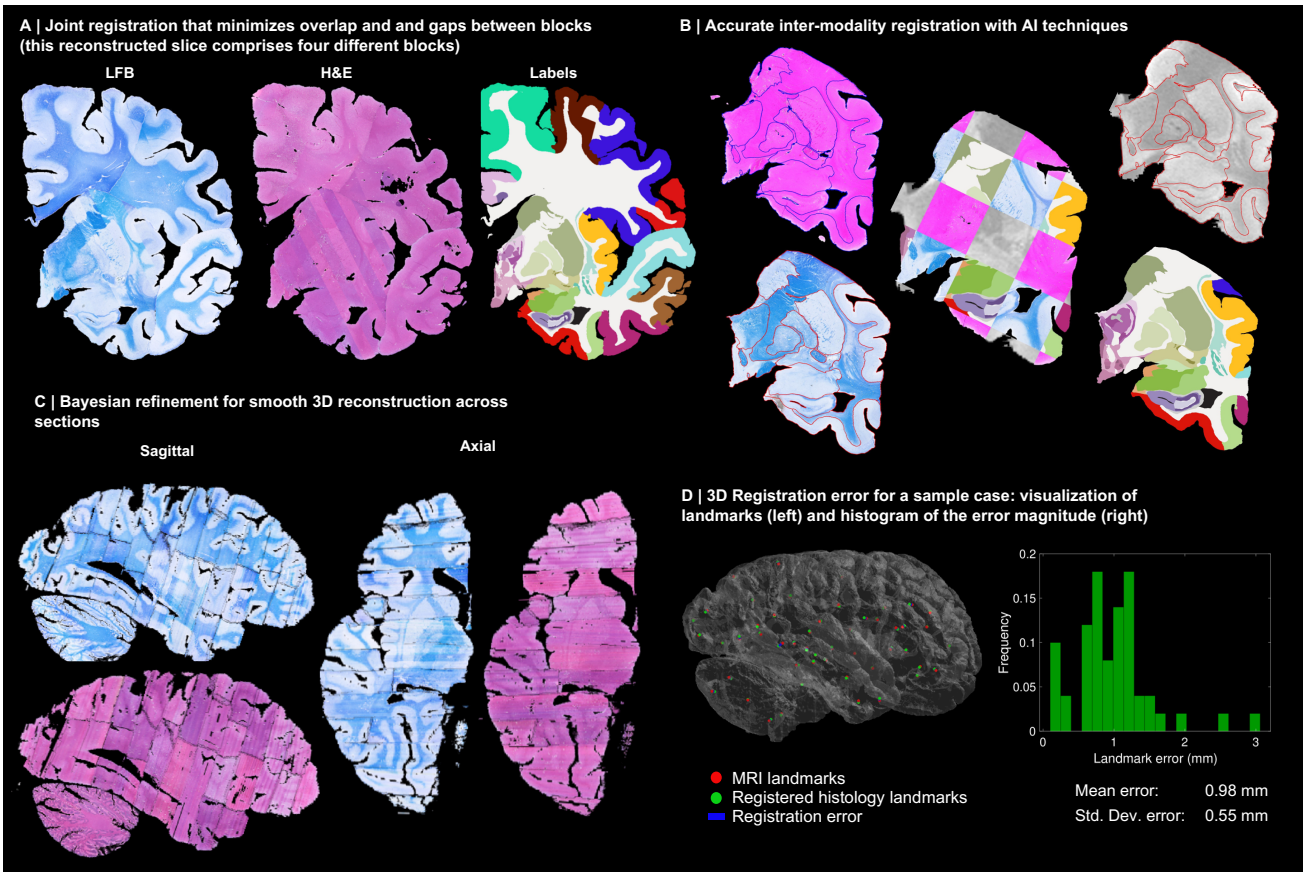

Extended Data Fig. 1: 3D reconstruction of Case 2. The visualisation follows the same convention as in Figure 2: (A) Coronal slice of the 3D reconstruction. (B) Mosaic of H&E, LFB, MRI, and segmentation, after our AI-enabled registration, with the contours of the ROIs overlaid. (C) Output of our Bayesian refinement algorithm for smooth 3D reconstruction of histology. (D) Visualization of 3D landmark registration error (left) and histogram of its magnitude (right).

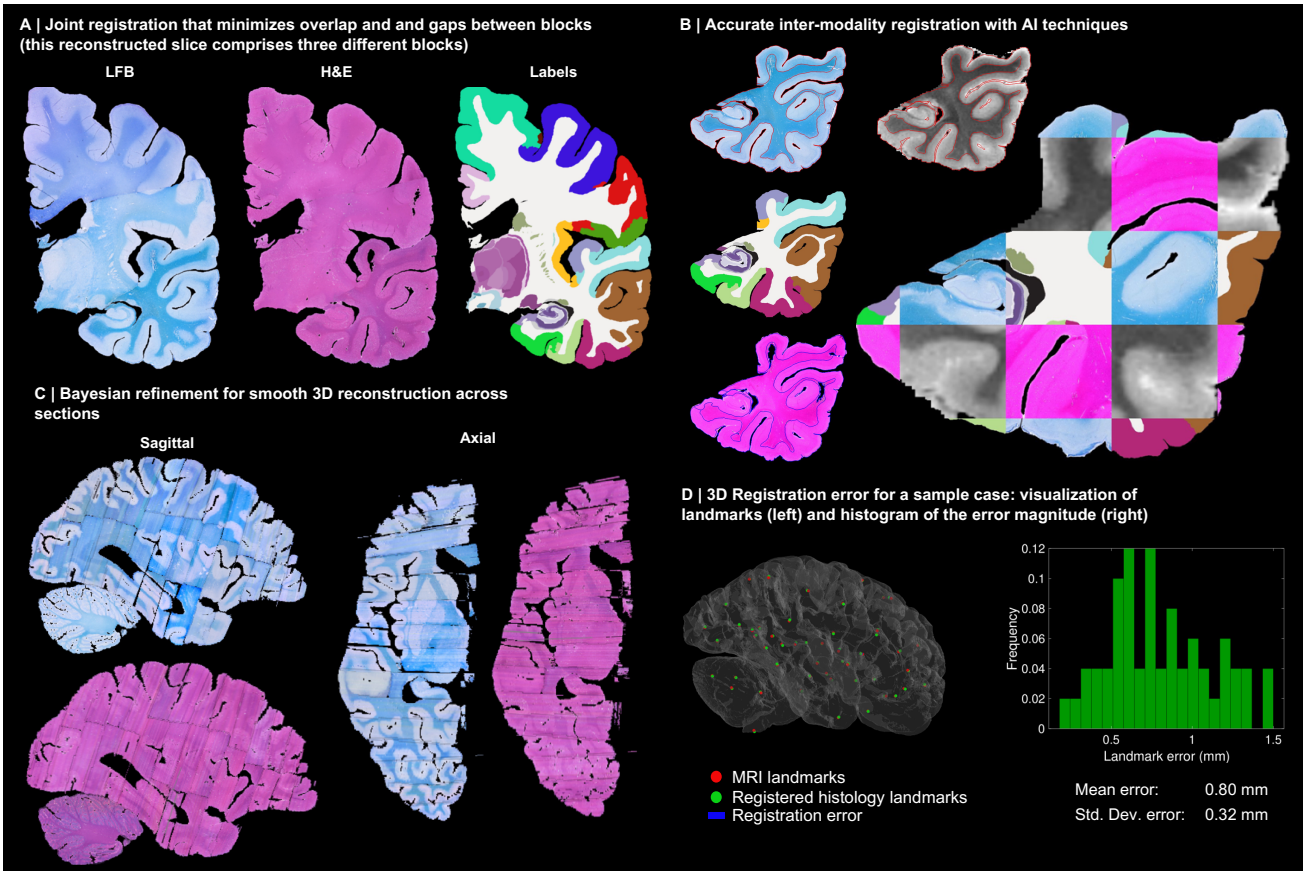

Extended Data Fig. 2: 3D reconstruction of Case 3. The visualisation follows the same convention as in Figure 2: (A) Coronal slice of the 3D reconstruction. (B) Mosaic of H&E, LFB, MRI, and segmentation, after our AI-enabled registration, with the contours of the ROIs overlaid. (C) Output of our Bayesian refinement algorithm for smooth 3D reconstruction of histology. (D) Visualization of 3D landmark registration error (left) and histogram of its magnitude (right).

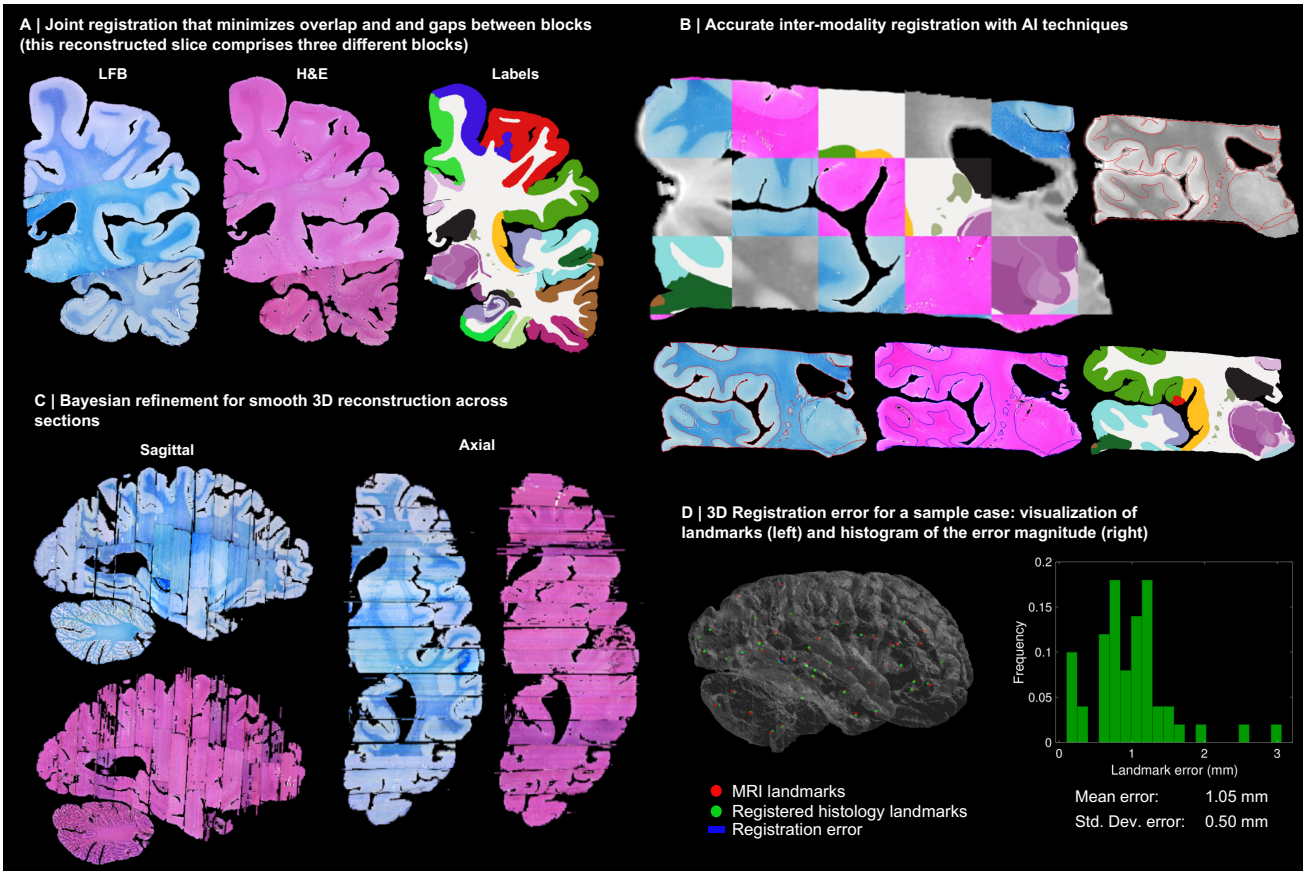

Extended Data Fig. 3: 3D reconstruction of Case 4. The visualisation follows the same convention as in Figure 2: (A) Coronal slice of the 3D reconstruction. (B) Mosaic of H&E, LFB, MRI, and segmentation, after our AI-enabled registration, with the contours of the ROIs overlaid. (C) Output of our Bayesian refinement algorithm for smooth 3D reconstruction of histology. (D) Visualization of 3D landmark registration error (left) and histogram of its magnitude (right).

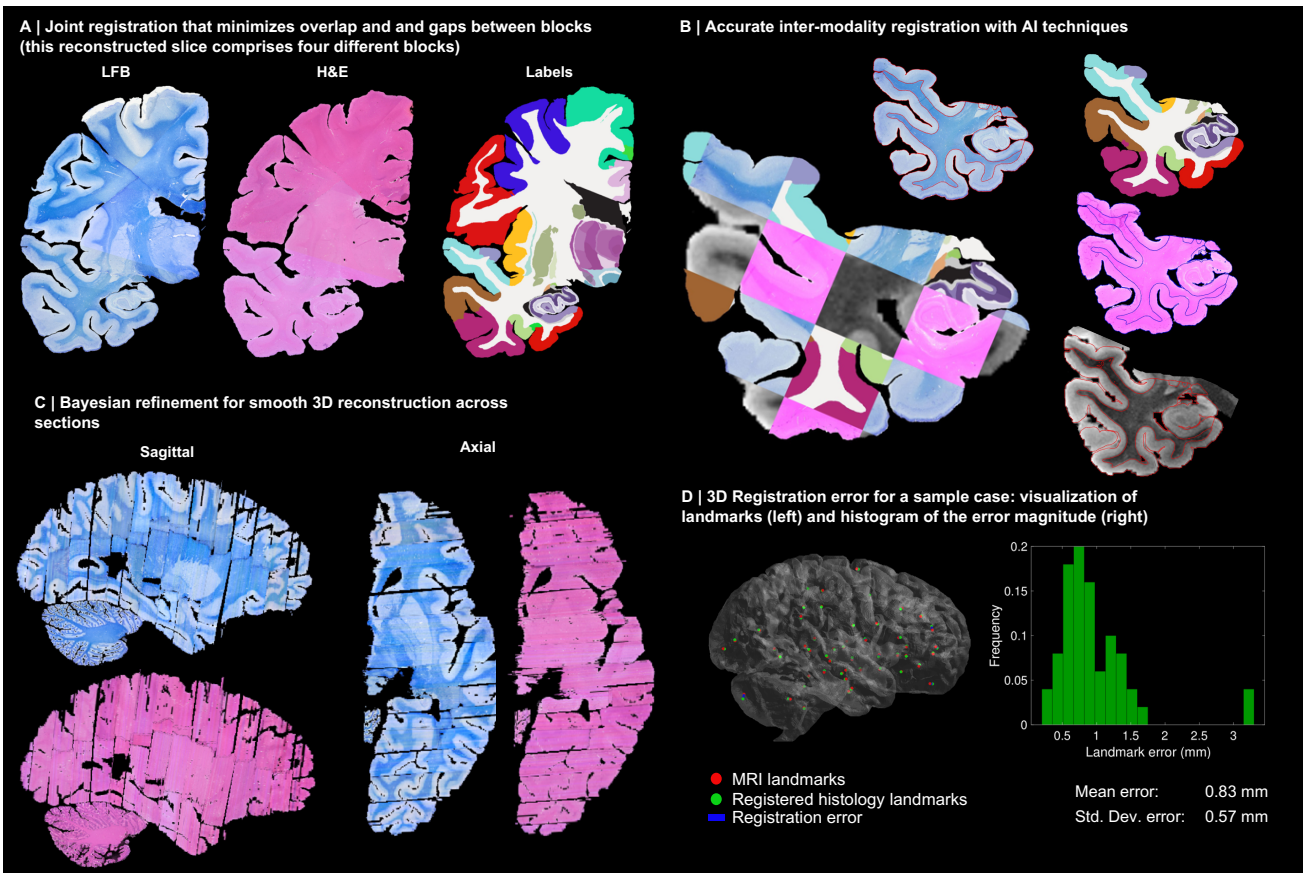

Extended Data Fig. 4: 3D reconstruction of Case 5. The visualisation follows the same convention as in Figure 2: (A) Coronal slice of the 3D reconstruction. (B) Mosaic of H&E, LFB, MRI, and segmentation, after our AI-enabled registration, with the contours of the ROIs overlaid. (C) Output of our Bayesian refinement algorithm for smooth 3D reconstruction of histology. (D) Visualization of 3D landmark registration error (left) and histogram of its magnitude (right).

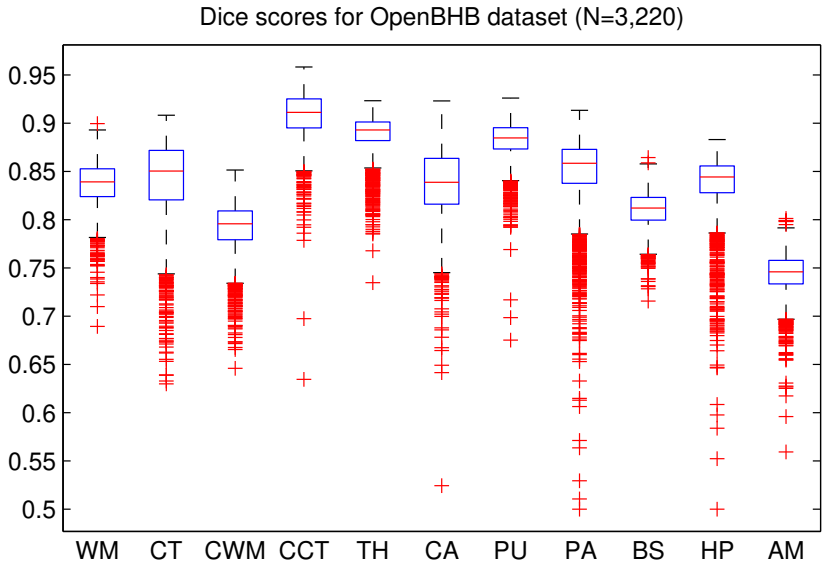

Extended Data Fig. 5: Box plots of the Dice scores of the automated segmentations computed with NextBrain on the OpenBHB dataset (3,330 subjects), using FreeSurfer segmentations as reference. The scores are computed at the whole regions level, i.e., the level of granularity at which FreeSurfer segments. On each box, the central mark indicates the median, the edges of the box indicate the 25th and 75th percentiles, the whiskers extend to the most extreme data points not considered outliers, and the outliers are plotted individually as '+'. The abbreviations for the regions are: WM = white matter of the cerebrum, CT = cortex of the cerebrum, CWM = cerebellar white matter, CCT = cerebellar cortex, TH = thalamus, CA = caudate, PU = putamen, PA = pallidum, BS = brainstem, HP = hippocampus, AM = amygdala.

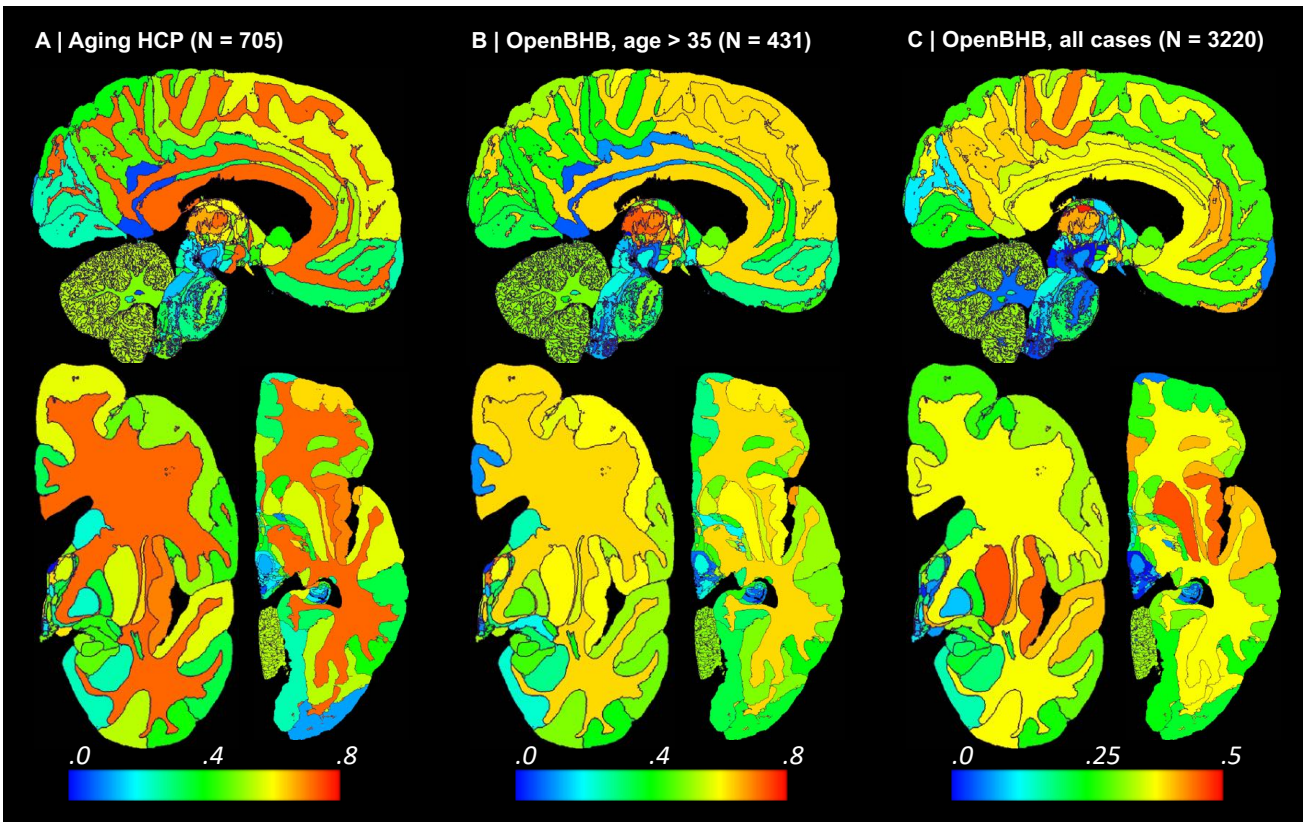

Extended Data Fig. 6: Absolute value of Spearman correlation for ROI volumes vs age derived from in vivo MRI scans (additional slices). The visualisation follows the same convention as in Figure 5: (A) Ageing HCP dataset. (B) OpenBHB dataset, restricted to ages over 35. (C) Full OpenBHB dataset.